Numerical Simulation of Blasting in Confined Fractured Rocks using an Immersed-Body Fluid-Solid Interaction Model

Pan Yang [a], Qinghua Lei [b,*], Jiansheng Xiang [a], John-Paul Latham [a], Christopher Pain [a]

[a] *Department of Earth Science and Engineering, Imperial College London, London, UK*

[b] *Department of Earth Sciences, ETH Zürich, Zürich, Switzerland*

[*] Correspondence: qinghua.lei@erdw.ethz.ch

Abstract:

We model blast-induced fracturing and fragmentation processes in fractured rocks using a fully coupled fluid-solid interaction model. This model links a finite-discrete element solid solver with a control volume-finite element fluid solver through an immersed-body method. The solid simulator can capture the deformation of intact rocks, interaction of matrix blocks, displacement of existing fractures and propagation of new cracks. The fluid simulator can simulate the highly compressible gas flow involved in the blasting and explosion process, which is assumed to follow the John-Wilkins-Lee equation of state. We design numerical experiments as follows. First, we generate a series of 1 m × 1 m discrete fracture networks associated with different fracture density and mean length values to consider various scenarios of distributed pre-existing fractures in rock. We apply isotropic/anisotropic in-situ stresses to the rock such that the system reaches an equilibrium state. Then we release the compressible gas associated with a prescribed high pressure in the borehole to simulate explosion, which engenders stress wave propagation and new crack generation in the system. We observe that the presence of natural fractures has a significant impact on the blast behaviour of fractured rocks such that new cracks tend to be arrested by pre-existing discontinuities which however accommodate wing cracks at their tips linking with other structures. Blast-driven cracks attempt to propagate along

the maximum principal stress direction if an anisotropic stress condition is imposed. Our research findings have important implications for the design and assessment of blasting for underground excavation in fractured formations.

Key words: blast; fractured rock; fluid-solid coupling; fracture propagation; fragmentation

1. Introduction

Fracturing and fragmentation of rock materials via explosive operations is often used in the civil and mining industry to facilitate underground excavation in geological media (Harrison and Hudson, 2000). In order to predict the blast performance and optimise the explosion design, engineers often adopt empirically-based rules (Chapman, 1899), which strongly rely on the users' experiences. Thus, some semi-analytical formulations supported by experimental data, e.g. the Kuz-Ram model (Cunningham, 1987), have been developed and incorporated into engineering analysis routines. For example, a range of fragmentation prediction models that consider the in-situ block size distribution have been discussed in the context of blasting for coastal engineering armour stone (Latham et al., 2006). Several analytical formulae have also been derived for calculating blast-driven fracture propagation in simple geometrical settings (Nilson et al., 1985; Paine and Please, 1994). Although these approaches provide very efficient solutions to estimating the blast behaviour of rocks, the understanding of underlying mechanisms and the analysis of complex geometries may require more sophisticated analysis using numerical models.

Over the past decades, many different numerical models have been developed to mimic blast-induced fracturing processes in rocks, which may be classified into two major types, i.e. the parted approach and the complete approach. The former group artificially separates the blast process into two distinct phases, i.e. the fragmentation phase involving fracture initiation and shock wave

propagation (Dehghan Banadaki and Mohanty, 2012; Ma and An, 2008), and the burden movement phase involving fracture extension and fragment transportation (Yan et al., 2016). The complete approach aims to capture the entire blasting process including detonation, shock wave propagation, compressible gas flow, fracture and fragmentation as well as solid-fluid interactions in a unified framework (Mohammadi and Bebamzadeh, 2005; Mohammadi and Pooladi, 2012, 2007; Morris et al., 2006; Ning et al., 2011b; Yang et al., 2017), rendering more realistic simulations compared to the parted approach.

To achieve complete blast modelling, three key components are needed, i.e. solid model, gas model and solid-fluid interaction model. Simulation of solid dynamics including vibration, fracture and fragmentation has been attempted using continuum-based damage mechanics models in the context of the finite element method (Hao et al., 2002; Liu and Katsabanis, 1997; Saharan and Mitri, 2008; Wei et al., 2009; Yang et al., 1996; Zhu et al., 2007). However, such continuum representations of fractures may not permit an easy capture of the important discontinuous behaviour such as fracture wall separation and gas penetration. To overcome such limitations, discontinuum-based fracture mechanics models, such as the discrete element method (Donzé et al., 1997; Onederra et al., 2013; Wang and Konietzky, 2009), discontinuous deformation analysis method (Ning et al., 2011b, 2011a), meshfree method (Rabczuk and Eibl, 2006), and hybrid finite-discrete element method (Mitelman and Elmo, 2014; Mohammadi and Bebamzadeh, 2005; Morris et al., 2006; Munjiza et al., 2000), have been used more frequently in simulating blast-induced fracturing in rocks. Regarding the gas flow simulation, the simplest way is to impose empirically-defined pressure profiles on the walls of blasting holes and/or the surfaces of induced fractures (Donzé et al., 1997; Ma and An, 2008; Ning et al., 2011b, 2011a; Saharan and Mitri, 2008; Zhu et al., 2007), which, however, cannot consider the

important time-dependent gas pressure variations. Thus, various gas models that solve fluid governing equations have been implemented in blast modelling, such as an one-dimensional pipe flow (Munjiza et al., 2000), a non-uniform isentropic gas model (Mohammadi and Pooladi, 2007) and a generalised inertia-dominated gas flow model (Yang et al., 2017), to more accurately calculate the pressure imposed on solid walls. With respect to the solid-fluid coupling, the gas flow and solid dynamics may be solved either based on a single mesh (Munjiza et al., 2000) or two separate meshes (Mohammadi and Bebamzadeh, 2005; Mohammadi and Pooladi, 2012). To better represent the viscous fluid behaviour (i.e. shear stress of fluids imposed on solid walls), a third mesh named "shell mesh" associated with a coupling term may need to be included (Viré et al., 2015; Yang et al., 2017, 2016). The use of shell mesh can significantly reduce the computational time because force transfer only needs to be solved on the shell mesh, which generally consists of a much smaller number of elements compared to the fluid or solid mesh. The shell mesh method also permits to incorporate complex boundary layer formulations (Yang et al., 2019).

By conducting blast numerical simulations, the influences of explosive charge, detonation style and boundary confinement as well as nearby faults on the blast-driven fracture development in rock have been extensively investigated in the literature (Donzé et al., 1997; Ma and An, 2008; Munjiza et al., 2000; Wang et al., 2009; Yang et al., 2017). However, crustal rocks are ubiquitously embedded with natural fractures (Bonnet et al., 2001), which may significantly dominate the dynamic response of the system and strongly affect the blast-driven crack growth, but very little investigation has been done to understand this problem apart from our preliminary study using regular discontinuity sets (Latham et al., 2017). Thus, in this paper, we aim to combine the state-of-the-art fluid-solid interaction simulation (Yang et al., 2017) with the discrete fracture network model (Lei et al., 2017a)

to gain insights into the role of pre-existing natural discontinuities in blasting processes in fractured geological media. We consider generic scenarios where a finite-sized fractured rock is confined by in-situ stresses and study the explosion out of a single borehole, while the communication between multiple blast holes is not analysed. We will elucidate the important effects of the geometrical properties of natural fractures (e.g. density and length) in conjunction with geomechanical conditions (e.g. stress magnitude and ratio). The remainder of the paper is organised as follows. Section 2 describes the governing equations and fundamental principles underpinning the solid, fluid and solid-fluid coupling solvers. Section 3 presents the setup of numerical models including the fracture network geometry, stress loading condition, and explosive operation, while the simulation results are further shown in Section 4. Finally, a brief discussion is given and conclusions are drawn in Section 5.

2. Methodology

We simulate the blast-induced fracturing and fragmentation processes in fractured rocks using a two-dimensional (2D) fully-coupled fluid-solid interaction model. This model combines a finite-discrete element solid model (Lei et al., 2017b, 2016; Xiang et al., 2009b, 2009a) with a control volume-finite element fluid model (Lei et al., 2018; Pain et al., 2001; Pavlidis et al., 2016; Xie et al., 2016) based on an immersed-body coupling framework (Viré et al., 2015, 2012; Yang et al., 2019, 2017, 2016). Both the solid and fluid models have been validated against laboratory experiments and analytical/empirical solutions in our past research (Farsi, 2017; Lei, 2016; Lei et al., 2018, 2016; Pavlidis et al., 2016; Xiang et al., 2009b; Xie et al., 2016). The validity and accuracy of this immersed-body coupling model has also been examined in our previous work against semi-analytical solutions, experimental data and other simulation tools (Viré et al., 2015, 2012; Yang et al., 2017, 2016); especially, the conservation of momentum and energy of the numerical model, which is

important for blast modelling, has been examined (Yang, 2018). In this paper, the computational domain consists of a fluid subdomain that fully immerses the solid subdomain (Fig. 1). The fundamental principles and governing equations for modelling solid dynamics, fluid dynamics and solid-fluid interactions involved in rock blasting processes are described successively in the following subsections.

2.1 Solid dynamics model

The solid dynamics is modelled using an open-source computational solid mechanics platform "Solidity" based on a hybrid finite-discrete element method (Xiang et al., 2009b, 2009a), which can realistically capture the stress evolution in intact rocks, interaction between matrix blocks, deformation of pre-existing fractures, and propagation of new cracks (Latham et al., 2013; Lei et al., 2017a). The solid model represents a 2D fractured rock using an unstructured, fully-discontinuous mesh of three-node triangular finite elements, which are linked by four-node joint elements (Fig. 2). There are two types of joint elements: unbroken joint elements inside the matrix and broken joint elements along fractures (Lei et al., 2016). The joint elements (either broken or unbroken) are created and embedded between the edges of triangular element pairs before the numerical simulation and no remeshing is performed during later computation.

The governing equation of the solid dynamics is given by:

$$\mathbf{F}_{\text{ext}} - \mathbf{F}_{\text{int}} + \mathbf{F}_{\text{f}} = \mathbf{M}_{\text{s}} \frac{\mathrm{d}\mathbf{u}_{\text{s}}}{\mathrm{d}t}, \tag{1}$$

where $\mathbf{M}$ is the lumped nodal mass matrix, $\mathbf{F}_{\text{int}}$ are the internal nodal forces induced by the deformation of triangular elements, $\mathbf{F}_{\text{ext}}$ are the external nodal forces including external loads $\mathbf{F}_{\text{l}}$ contributed by boundary conditions and body forces, cohesive bonding forces $\mathbf{F}_{\text{b}}$ caused by the deformation of unbroken joint elements, and contact forces $\mathbf{F}_{\text{c}}$ generated by the contact interaction via

broken joint elements, $\mathbf{F}_f$ is the solid-fluid exchange force dependent on the gas pressure and viscosity, $\mathbf{u}_s$ is the solid velocity, and t is the time. The deformation of intact rocks is captured by linear-elastic constant-strain finite elements with the continuity constrained by the bonding forces of unbroken joint elements (Munjiza et al., 1999). The interaction of discrete solid bodies is calculated based on the penetration of finite elements via broken joint elements (Munjiza and Andrews, 2000). The elasto-plastic fracturing in formation rocks is modelled by a smeared crack (i.e. cohesive zone) method that can capture the non-linear stress-strain behaviour of the plastic zone ahead of each fracture tip (Munjiza et al., 1999). The fracture propagation model can consider both tensile and shear failure in brittle (or quasi-brittle) rocks governed by specific mode I and II energy release rates (Lei, 2016). The equations of motion of the solid model are solved through an explicit time integration scheme based on the forward Euler method.

2.2 Fluid dynamics model

The compressible gas flow is simulated using an open-source computational fluid dynamics platform "Fluidity" based on a mixed control volume-finite element method (Pavlidis et al., 2016; Xie et al., 2016). The continuity equation for the compressible gas flow is written as:

$$\frac{\partial \rho_f}{\partial t} + \nabla \cdot (\rho_f \mathbf{u}_f) = 0 , \tag{2}$$

where, ρ_f and $\mathbf{u}_f$ are the fluid density and velocity, respectively. The momentum equation is written as:

$$\frac{\partial}{\partial t}(\rho_f \mathbf{u}_f) + \nabla \cdot (\rho_f \mathbf{u}_f \otimes \mathbf{u}_f + p - \boldsymbol{\tau}) = \rho_f \mathbf{F}_b + \mathbf{s}_c , \tag{3}$$

where $\mathbf{F}_b$ is the body or internal force per unit mass (e.g. gravity), p is the fluid pressure, $\boldsymbol{\tau}$ is the shear stress and the $\mathbf{s}_c$ is the solid-to-fluid coupling term. The energy equation is given as:

$$\frac{\partial}{\partial t}(\rho_f E) + \nabla \cdot (\rho_f E \mathbf{u}_f - \boldsymbol{\tau} \mathbf{u}_f + \mathbf{q}) = \rho_f \mathbf{F}_b \mathbf{u}_f , \tag{4}$$

where $\mathbf{q}$ is the rate of volumetric heat increment per unit mass, $E = e + |\mathbf{u}|^2/2$ is the total specific

155 energy, and e is the internal energy per unit mass.

156 The following supplementary equation is introduced to link the solid and fluid governing
157 equations:

158 $$\hat{\sigma}(\hat{\mathbf{u}}^{\mathrm{f}} - \mathbf{u}_{\mathrm{f}}^{\mathrm{f}}) = \hat{\sigma}(\hat{\mathbf{u}}_{\mathrm{s}}^{\mathrm{s}} - \mathbf{u}_{\mathrm{f}}^{\mathrm{s}}), \tag{5}$$

159 where $\hat{\sigma} = \rho_{\mathrm{f}} / \Delta t$, $\hat{\mathbf{u}}^{\mathrm{f}} = \alpha_{\mathrm{f}}\mathbf{u}_{\mathrm{f}}^{\mathrm{f}} + \alpha_{\mathrm{s}}\mathbf{u}_{\mathrm{s}}^{\mathrm{f}} = \hat{\mathbf{u}}_{\mathrm{f}}^{\mathrm{f}} + \hat{\mathbf{u}}_{\mathrm{s}}^{\mathrm{f}}$, and α_{f} and α_{s} denote the fluid and solid volume
160 fraction, respectively. Note that the subscripts and superscripts indicate the field and mesh,
161 respectively ("f" is for fluid and "s" is for solid). Hence, the continuity equation for the superimposed
162 fluid-solid domain is rewritten as:

163 $$\nabla \cdot \hat{\mathbf{u}} = \upsilon, \tag{6}$$

164 where:

165 $$\hat{\mathbf{u}}^{\mathrm{f}} = \begin{cases} \mathbf{u}_{\mathrm{f}}^{\mathrm{f}} & \text{when} \quad \alpha_{\mathrm{f}} = 1, \quad \alpha_{\mathrm{s}} = 0; \\ \mathbf{u}_{\mathrm{s}}^{\mathrm{f}} & \text{when} \quad \alpha_{\mathrm{f}} = 0, \quad \alpha_{\mathrm{s}} = 1. \end{cases} \tag{7}$$

166 We use the John-Wilkins-Lee (JWL) equation of state (Kury et al., 1999; Tarver et al., 1997) to
167 describe the thermodynamic relationship of fluids that links the fluid temperature, pressure, density
168 and internal energy to close the fluid governing equations. The JWL equation is written as:

169 $$p = A\left(1 - \frac{\omega}{R_1 V}\right)e^{-R_1 V} + B\left(1 - \frac{\omega}{R_2 V}\right)e^{-R_2 V} + \frac{\omega e_0}{V}, \tag{8}$$

170 where A, B, R_1, R_2, ω and e_0 are experimentally-fitted material constants, p is the pressure, $V = \rho_e/\rho_f$ is
171 the relative volume. We assume an isothermal condition such that the internal energy e in the energy
172 equation, i.e. Eq. (4), remains constant.

173 **2.3 Solid-fluid interaction model**

174 The fluid and solid solvers are fully coupled within the framework of an immersed-body method
175 (Viré et al., 2015, 2012; Yang et al., 2016). After the gas pressure p and velocity $\mathbf{u}_{\mathrm{f}}^{\mathrm{f}}$ are solved from

Eqs. (4), (5) and (7) based on the fluid mesh, they are projected onto the solid surface via the shell mesh (Fig. 3), with the exchange force $\mathbf{F}_\mathrm{f}$ calculated as:

$$\mathbf{F}_\mathrm{f} = \int_{\Gamma_\mathrm{solid}} N_i n \cdot (\boldsymbol{\tau} + \mathbf{I}p) \mathrm{d}\Gamma, \tag{9}$$

where Γ_solid represents the solid surface, N_i is the shape function, n is the outward normal, and $\mathbf{I}$ is the identity matrix. We decompose the term $\int_{\Gamma_\mathrm{solid}} N_i n \cdot \boldsymbol{\tau} \mathrm{d}\Gamma$ based on the directions of the 2D velocity components, i.e. u and v, as:

$$\int_{V_\mathrm{shell}} N_i \left(a_{\mathrm{xx}} u_\mathrm{sl} + a_{\mathrm{xy}} v_\mathrm{sl} \right) \mathrm{d}V \quad \text{and} \quad \int_{V_\mathrm{shell}} N_i \left(a_{\mathrm{yx}} u_\mathrm{sl} + a_{\mathrm{yy}} v_\mathrm{sl} \right) \mathrm{d}V, \tag{10}$$

where V_shell stands for the volume of the shell mesh and $\mathbf{u}_\mathrm{sl} = [u_\mathrm{sl}, v_\mathrm{sl}] = \mathbf{u}_\mathrm{s} - \mathbf{u}_\mathrm{f}$ is the slip velocity. The coefficient $\mathbf{a} = [a_{\mathrm{xx}}, a_{\mathrm{xy}}, a_{\mathrm{yx}}, a_{\mathrm{yy}}]$ is given as:

$$\begin{aligned}
a_{\mathrm{xx}} &= \frac{\mu_\mathrm{t}}{\Delta r \Delta x_\mathrm{wall}} [n_\mathrm{x} \frac{4}{3} n_\mathrm{x} + n_\mathrm{y} n_\mathrm{y}]; \\
a_{\mathrm{xy}} &= \frac{\mu_\mathrm{t}}{\Delta r \Delta x_\mathrm{wall}} [-n_x \frac{2}{3} n_\mathrm{y} + n_\mathrm{y} n_\mathrm{x}]; \\
a_{\mathrm{yx}} &= \frac{\mu_\mathrm{t}}{\Delta r \Delta x_\mathrm{wall}} [n_\mathrm{x} n_\mathrm{y} - n_\mathrm{x} \frac{2}{3} n_\mathrm{y}]; \\
a_{\mathrm{yy}} &= \frac{\mu_\mathrm{t}}{\Delta r \Delta x_\mathrm{wall}} [n_\mathrm{x} n_\mathrm{x} + n_\mathrm{y} \frac{4}{3} n_\mathrm{y}],
\end{aligned} \tag{11}$$

where $\Delta r = (0.1\sim1) \cdot \Delta x_\mathrm{wall}$ the thickness of the shell with Δx_wall being the fluid mesh size near the solid surface, and μ_t is the dynamic viscosity.

The exchange force $\mathbf{F}_\mathrm{f}$ is substituted into Eq. (1) to compute the solid velocity, based on which the coupling term $\mathbf{s}_\mathrm{c}$ can be eventually derived as:

$$\begin{aligned}
s^\mathrm{f}_{\mathrm{c,x}} &= a_{\mathrm{xx}} u_\mathrm{s} + a_{\mathrm{xy}} v_\mathrm{s}; \\
s^\mathrm{f}_{\mathrm{c,y}} &= a_{\mathrm{yx}} u_\mathrm{s} + a_{\mathrm{yy}} v_\mathrm{s},
\end{aligned} \tag{12}$$

and further substituted into Eq. (3). The mass conservation between the fluid and solid domains is achieved through a conservative Galerkin projection-based mesh interpolation (Farrell and Maddison, 2011). The solid-fluid coupling in the context of the immersed-body method is numerically achieved

194 by linking the solid simulator Solidity and fluid simulator Fluidity with the governing equations
195 solved interactively and iteratively in a time-marching scheme (see the flow chart given in Fig. 4).

196 **3. Model setup**

197 We use the discrete fracture network approach (Lei et al., 2017a) to represent the geometrical
198 distribution of natural fractures in a 1 m × 1 m square domain of rock. We assume that the probability
199 density function of fracture trace lengths follows a negative exponential distribution (Priest and
200 Hudson, 1981):

201 $$f(l) = \frac{1}{\zeta} e^{-l/\zeta} \tag{13}$$

202 where l is the fracture length and ζ is the mean length. The negative exponential distribution
203 characterises the important feature of natural fracture systems that large fractures have low frequency
204 while small fractures have high frequency (Davy, 1993). The location and orientation of fractures are
205 assumed purely random. We explore two different cases of fracture density (i.e. number of fractures per
206 area), i.e. N = 50 and 100 m^{-2} (referred hereafter as low and high density cases, respectively), and three
207 different values of the mean length, i.e. ζ = 0.1, 0.2 and 0.3 m (Fig. 5). To facilitate comparison, the
208 high density fracture network is created by superimposing new fractures onto the low density pattern;
209 the high and low mean length cases have the same facture centre locations.

210 The rock mass properties are given as follows. The bulk density is 2680 kg/m^3, the Young's
211 modulus is 60.0 GPa, the Poisson's ratio is 0.25, the internal friction angle is 31˚, the tensile strength
212 is 15.0 MPa, the cohesive strength is 55.0 MPa, the residual friction angle is 31˚, and the mode I and
213 II energy release rates are 74.3 and 88.4 J/m^2, respectively.

214 The fractured rock first reaches to equilibrium under an imposed isotropic (S_x = S_y = 1.0 MPa) or
215 anisotropic (S_x = 3.0 MPa, S_y = 1.0 MPa) stress loading condition. The in-situ stress level is very low

compared to the intact rock strength such that no cracks are generated during the model equilibrium stage. We then release the compressible gas associated with a prescribed high initial pressure (P_0 = 50 MPa) inside the central borehole (with a diameter of 0.1 m) to initiate explosion, which leads to shock wave propagation and new fracture generation across the domain. An absorptive layer with increased density and reduced modulus is placed surrounding the fractured domain to slow down stress waves such that the simulation is terminated before any reflection waves coming back to the domain.

In the simulations of this work, we choose the maximum and minimum fluid element sizes as 0.02 m and 0.005 m, respectively, and the solid element size as 0.01 m. The mesh setting here is the same as that in our previous work studying blasting in intact rocks (Yang et al., 2017), which gives simulation results consistent to other published research in the literature with respect to borehole gas pressure history (Mohammadi and Pooladi, 2012) and rock fragmentation pattern (Munjiza et al., 2000). Furthermore, the shell thickness is chosen as 1/10 of the minimum fluid element size, according to our previous sensitivity analysis results (Yang et al., 2016). The time step for both fluid and solid solvers is set to be 0.25×10^{-7} s, which is smaller than the time step used in our previous work (Yang et al., 2017), to ensure the model convergence for simulating blasting in prefractured rocks. The runtime of each simulation is about 650 hours on a desktop computer equipped with an Intel(R) Xeon(R) CPU E5-2697@2.30 GHz).

4. Results

4.1 Isotropic stress confinement

Figs. 6 and 7 give the distribution of local maximum principal stresses and the variation of fracture network geometries at different time stages (i.e. t = 0.08, 0.16, 0.24 ms) after the explosion in the low-density fracture networks of different mean length values subjected to the isotropic stress loading

condition ($S_x = S_y = 1.0$ MPa). The stress wave propagates radially with a circular outer front (see t = 0.08 ms). When the mean length is small, the high stress zone around the borehole exhibits a quite isotropic pattern, like in isotropic, homogeneous materials, because the effect of pre-existing fractures is minor. The blast-induced new cracks (mainly tension-dominated) initiating from the central borehole tend to exhibit an isotopically growth manner: some may propagate straight without meeting any fracture or even cross pre-existing structures, while others link with pre-existing fractures and generate wing cracks at their far-end tips (Fig. 7). However, as the mean fracture length increases, the influence of natural fractures on the stress wave propagation becomes significant, as can be seen from the high stress zone formed on one side of some large fractures (Fig. 6). This is because shear stress cannot be fully transferred to the opposite side of these fractures that can either open or slip. The distribution of local stresses thus exhibits strong heterogeneity features. The new cracks, which are mostly tension-dominated, seem to only develop in the region with less pre-existing fractures, while in other areas only minor small cracks are generated to link pre-existing discontinuities (Fig. 7). Furthermore, most new cracks initiating from the borehole are arrested by pre-existing structures. Some localised fragmentation seems to emerge at the intersection of pre-existing fractures in the networks of a larger mean length with more fracture interconnections involved.

Figs. 8 and 9 give the distribution of local maximum principal stresses and the variation of fracture network geometries in the high-density fracture networks subjected to the isotropic stress loading condition. The influence of natural fractures with a small mean length on the shock wave propagation (Fig. 8) and blast-driven new crack formation seems to be still minor (Fig. 9), although more fracture coalescence occurs compared to that in the low-density case. However, if the mean fracture length is long, the system of natural fractures becomes well connected, allowing only a few wing cracks to

propagate from the tips of some pre-existing fractures under dynamic vibrations. Furthermore, intense fragmentation tends to locally occur at the junction of some large fractures that intersect with each other at a small acute angle and also connect to the borehole, where significantly shear and rotation are accommodated.

Fig. 10 shows the directional distribution of cumulative length of blast-induced cracks in the isotropically stressed fractured rocks. It seems that with the increase of mean length of pre-existing fractures, the total length of new cracks decreases. Furthermore, in the high-density fracture networks, the new cracks propagate more isotropically under the isotropic stress loading, whist the new cracks in the low-density fracture networks exhibit slight directional preference due to the influence of local pre-existing fractures around the borehole.

4.2 Anisotropic stress confinement

Figs. 11 and 12 give the variation of local maximum principal stresses and fracture patterns at different time stages (i.e. t = 0.08, 0.16, 0.24 ms) after the explosion in the low-density fracture networks subjected to the anisotropic stress loading condition (S_x = 3.0 MPa, S_y = 1.0 MPa). It can be seen that the stress wave front is significantly distorted at the location of pre-existing fractures (see t = 0.08 ms) because of the slip movement of these discontinuities (Fig. 11). The blast-induced new cracks, especially those wing cracks initiating from the tips of pre-existing fractures, tend to propagate aligning the direction of the maximum principal stress, i.e. x direction (Fig. 12). With the increase of the mean length of pre-existing fractures, the distortion of the stress wave front becomes more manifest, the propagation of new cracks is more obstructed by other discontinuities, and more concentrated breakage emerges at fracture intersections, due to the effects of more interconnected pre-existing fractures.

Figs. 13 and 14 show the variations of local maximum principal stresses and fracture network

patterns in the high-density fracture networks subjected to the anisotropic stress state. The stress wave field is strongly distorted, especially in the highly connected fracture network of $\zeta = 0.3$ m where the wave front becomes very obscure (see $t = 0.08$ ms) (Fig. 13). The propagation of blast-induced cracks is strongly inhibited by interconnected pre-existing fractures, which however permit wing crack growing from their tips and linking with other structures (Fig. 14). In the network of $\zeta = 0.3$ m, an inner crushed zone of intense fracturing and fragmentation is formed, probably due to the reduced rock mass strength with highly connected fractures and the enhanced mean stress level. Some shear-dominated cracks also emerge inside the crushed zone. The crushing zone also tends to be bounded by pre-existing fractures surrounding the borehole; outside the crushed zone, only some minor wing cracks are accommodated.

Fig. 15 shows the directional distribution of cumulative length of blast-induced cracks in the anisotropically stressed fractured rocks. When the mean length of pre-existing fractures is small, the orientation preference of new cracks is evident, i.e. along the x direction where the maximum principal stress is imposed. With the increase of the mean length, the orientation preference seems to be attenuated due to the increased control of pre-existing fractures. In the high-density network with $\zeta = 0.3$ m, much more cracks (mostly located in the crushed zone) are generated but no favourite direction is shown.

5. Discussion and conclusions

The effects of fracture network properties such as density, length and connectivity on the hydraulic and geomechanical behaviour of fractured rocks have been extensively studied in the past (Davy et al., 2006; de Dreuzy et al., 2001; Lei et al., 2017b; Lei and Gao, 2018). If the system is well connected, the strength of the system is significantly reduced while the permeability is largely increased. In this paper, we observe that the connectivity of pre-existing fractures, which can be

304 enhanced by increasing either the fracture density or length, plays an important role in blast-induced
305 fracture propagation and rock fragmentation behaviour. When the fracture network is disconnected,
306 the blast energy causes new cracks radiating from the blast hole and wing cracks emanating from the
307 tips of pre-existing fractures. When the fracture network becomes more connected, the blast-induced
308 radial/wing cracks get arrested by pre-existing structures such that the blast energy is more dissipated
309 by the movements of fracture walls. In addition to the geometrical effects, we also elucidated the
310 important geomechanical influence, i.e. in-situ stress condition, on blast performance of fractured
311 rocks. An anisotropic stress loading tends to guide cracks to evolve preferentially along the direction
312 of the imposed maximum principal stress, while an isotropic stress loading seems to lead to an
313 isotropic growth manner. Our observation of stress-induced blast anisotropy shows consistency with
314 previous work that focused on blast in intact rocks (Donzé et al., 1997; Ma and An, 2008).
315 Furthermore, enhanced stress level and reduced rock mass strength may promote the formation of a
316 crushed zone around the blast hole, which has also been observed in many other simulation studies
317 which also only focused on intact rocks (Donzé et al., 1997; Mitelman and Elmo, 2014; Saharan and
318 Mitri, 2008; Zhu et al., 2007). Our paper advanced the current understanding of blast in rock materials
319 by considering the non-trivial interaction effects of pre-existing fractures in conjunction with the
320 important geomechanical impacts of in-situ stresses. It is worth mentioning that, in this paper, we
321 focused on the analysis of stress and fracture pattern evolution while the gas pressure field is not
322 shown although the gas flow is solved in our simulation. The reader is referred to our previous work
323 for more detailed analysis of the gas field evolution during blast processes (Latham et al., 2017; Yang
324 et al., 2017).

325 To conclude, we conduced fully-coupled fluid-solid interaction simulation of blasting processes

326 in fractured rocks and investigated the mutual effects of natural fractures and in-situ stresses on the
327 blast-driven fracturing and fragmentation in rock materials. In disconnected fracture networks, blast
328 causes radial cracks initiating from the borehole and propagating in a quite sustained manner with
329 support from isolated pre-existing fractures and newly generated wing cracks. With the increase of
330 density and/or length of natural fractures, blast-induced new cracks tend to be arrested by pre-existing
331 structures, which only permit some wing crack growth emanating from their tips in order to
332 coalescence with other discontinuities. New cracks tend to propagate with no directional preference in
333 the rock under an isotropic stress loading but become more aligned along the maximum principal
334 stress direction if an anisotropic boundary confinement is imposed. Elevated stress level and increased
335 fracture network connectivity may also lead to the formation of a crushed zone around the blast hole
336 and bounded by pre-existing fractures. Our research findings highlight the important role of natural
337 fractures in transitioning the blast fragmentation behaviour of fractured rocks from radial
338 cracking-dominated to fracture coalescence-dominated regimes, which have important implications
339 for the design and assessment of blasting performance of fractured geological formations for
340 tunnelling and underground excavation.

341 **References**

342 Bonnet, E., Bour, O., Odling, N.E., Davy, P., Main, I., Cowie, P., Berkowitz, B., 2001. Scaling of
343 fracture systems in geological media. Rev. Geophys. 39, 347–383.
344 https://doi.org/10.1029/1999RG000074
345 Chapman, D.L., 1899. On the rate of explosion in gases. London, Edinburgh, Dublin Philos. Mag. J.
346 Sci. 47, 90–104. https://doi.org/10.1080/14786449908621243
347 Cunningham, C.V.B., 1987. Fragmentation estimations and Kuz–Ram model-four years on, in:
348 Fourney, W.L., Dick, R.D. (Eds.), The 2nd International Symposium on Rock Fragmentation by
349 Blasting. Keystone, Colorado, pp. 475–487.

Davy, P., 1993. On the frequency-length distribution of the San Andreas Fault System. J. Geophys. Res. 98, 12141–12151. https://doi.org/10.1029/93JB00372

Davy, P., Bour, O., de Dreuzy, J.-R.J.-R., Darcel, C., 2006. Flow in multiscale fractal fracture networks, in: Cello, G., Malamud, B.D. (Eds.), Fractal Analysis for Natural Hazards. Geological Society, London, Special Publications, London, pp. 31–45. https://doi.org/10.1144/GSL.SP.2006.261.01.03

de Dreuzy, J.-R., Davy, P., Bour, O., 2001. Hydraulic properties of two-dimensional random fracture networks following a power law length distribution: 1. Effective connectivity. Water Resour. Res. 37, 2065–2078. https://doi.org/10.1029/2001WR900011

Dehghan Banadaki, M.M., Mohanty, B., 2012. Numerical simulation of stress wave induced fractures in rock. Int. J. Impact Eng. 40–41, 16–25. https://doi.org/10.1016/j.ijimpeng.2011.08.010

Donzé, F.V., Bouchez, J., Magnier, S.A., 1997. Modeling fractures in rock blasting. Int. J. Rock Mech. Min. Sci. 34, 1153–1163. https://doi.org/10.1016/S1365-1609(97)80068-8

Farrell, P.E., Maddison, J.R., 2011. Conservative interpolation between volume meshes by local Galerkin projection. Comput. Methods Appl. Mech. Eng. 200, 89–100. https://doi.org/10.1016/j.cma.2010.07.015

Farsi, A., 2017. Numerical and experimental investigations of particle stress and fracture for complex-shaped pellets (PhD thesis). Imperial College London, London.

Hao, H., Wu, C., Zhou, Y., 2002. Numerical analysis of blast-induced stress waves in a rock mass with anisotropic continuum damage models, Part 1: equivalent material property approach. Rock Mech. Rock Eng. 35, 79–94. https://doi.org/10.1007/s006030200012

Harrison, J.P., Hudson, J.A., 2000. Engineering Rock Mechanics: Part 2: Illustrative Worked Examples. Elsevier, Oxford. https://doi.org/10.1016/B978-0-08-043010-2.X5000-X

Kury, J.W., Don Breithaupt, R., Tarver, C.M., 1999. Detonation waves in trinitrotoluene. Shock Waves 9, 227–237. https://doi.org/10.1007/s001930050160

Latham, J.-P., Van Meulen, J., Dupray, S., 2006. Prediction of fragmentation and yield curves with reference to armourstone production. Eng. Geol. 87, 60–74. https://doi.org/10.1016/j.enggeo.2006.05.005

Latham, J.-P., Xiang, J., Belayneh, M., Nick, H.M., Tsang, C.-F., Blunt, M.J., 2013. Modelling stress-dependent permeability in fractured rock including effects of propagating and bending

fractures. Int. J. Rock Mech. Min. Sci. 57, 100–112. https://doi.org/10.1016/j.ijrmms.2012.08.002

Latham, J.-P., Yang, P., Lei, Q., Obeysekara, A., Salinas, P., Pavlidis, D., Xiang, J., Pain, C.C., 2017. Blast fragmentation in rock with discontinuities using an equation of state gas model coupled to a transient dynamics fracturing and fragmenting FEMDEM code, in: 51st US Rock Mechanics/Geomechanics Symposium. San Francisco, USA, p. ID703.

Lei, Q., 2016. Characterisation and modelling of natural fracture networks: geometry, geomechanics and fluid flow (PhD thesis). Imperial College London, London.

Lei, Q., Gao, K., 2018. Correlation between fracture network properties and stress variability in geological media. Geophys. Res. Lett. 45, 3994–4006. https://doi.org/10.1002/2018GL077548

Lei, Q., Latham, J.-P., Tsang, C.-F., 2017a. The use of discrete fracture networks for modelling coupled geomechanical and hydrological behaviour of fractured rocks. Comput. Geotech. 85, 151–176. https://doi.org/10.1016/j.compgeo.2016.12.024

Lei, Q., Latham, J.-P., Xiang, J., 2016. Implementation of an empirical joint constitutive model into finite-discrete element analysis of the geomechanical behaviour of fractured rocks. Rock Mech. Rock Eng. 49, 4799–4816. https://doi.org/10.1007/s00603-016-1064-3

Lei, Q., Latham, J.-P., Xiang, J., Tsang, C.-F., 2017b. Role of natural fractures in damage evolution around tunnel excavation in fractured rocks. Eng. Geol. 231, 100–113. https://doi.org/10.1016/j.enggeo.2017.10.013

Lei, Q., Xie, Z., Pavlidis, D., Salinas, P., Veltin, J., Matar, O.K., Pain, C.C., Muggeridge, A.H., Gyllensten, A.J., Jackson, M.D., 2018. The shape and motion of gas bubbles in a liquid flowing through a thin annulus. J. Fluid Mech. 855, 1017–1039. https://doi.org/10.1017/jfm.2018.696

Liu, L., Katsabanis, P.D., 1997. Development of a continuum damage model for blasting analysis. Int. J. Rock Mech. Min. Sci. 34, 217–231. https://doi.org/10.1016/S0148-9062(96)00041-1

Ma, G.W., An, X.M., 2008. Numerical simulation of blasting-induced rock fractures. Int. J. Rock Mech. Min. Sci. 45, 966–975. https://doi.org/10.1016/j.ijrmms.2007.12.002

Mitelman, A., Elmo, D., 2014. Modelling of blast-induced damage in tunnels using a hybrid finite-discrete numerical approach. J. Rock Mech. Geotech. Eng. 6, 565–573. https://doi.org/10.1016/j.jrmge.2014.09.002

Mohammadi, S., Bebamzadeh, A., 2005. A coupled gas–solid interaction model for FE/DE simulation

410 of explosion. Finite Elem. Anal. Des. 41, 1289–1308. https://doi.org/10.1016/j.finel.2005.03.002
411 Mohammadi, S., Pooladi, A., 2012. A two-mesh coupled gas flow–solid interaction model for 2D
412 blast analysis in fractured media. Finite Elem. Anal. Des. 50, 48–69.
413 https://doi.org/10.1016/j.finel.2011.08.016
414 Mohammadi, S., Pooladi, A., 2007. Non-uniform isentropic gas flow analysis of explosion in
415 fractured solid media. Finite Elem. Anal. Des. 43, 478–493.
416 https://doi.org/10.1016/j.finel.2006.11.005
417 Morris, J.P., Rubin, M.B., Block, G.I., Bonner, M.P., 2006. Simulations of fracture and fragmentation
418 of geologic materials using combined FEM/DEM analysis. Int. J. Impact Eng. 33, 463–473.
419 https://doi.org/10.1016/j.ijimpeng.2006.09.006
420 Munjiza, A., Andrews, K.R.F., 2000. Penalty function method for combined finite-discrete element
421 systems comprising large number of separate bodies. Int. J. Numer. Methods Eng. 49, 1377–
422 1396. https://doi.org/10.1002/1097-0207(20001220)49:11<1377::AID-NME6>3.0.CO;2-B
423 Munjiza, A., Andrews, K.R.F., White, J.K., 1999. Combined single and smeared crack model in
424 combined finite-discrete element analysis. Int. J. Numer. Methods Eng. 44, 41–57.
425 https://doi.org/10.1002/(SICI)1097-0207(19990110)44:1<41::AID-NME487>3.0.CO;2-A
426 Munjiza, A., Latham, J.P., Andrews, K.R.F., 2000. Detonation gas model for combined finite-discrete
427 element simulation of fracture and fragmentation. Int. J. Numer. Methods Eng. 49, 1495–1520.
428 https://doi.org/10.1002/1097-0207(20001230)49:12<1495::AID-NME7>3.0.CO;2-5
429 Nilson, R.H., Proffer, W.J., Duff, R.E., 1985. Modelling of gas-driven fractures induced by propellant
430 combustion within a borehole. Int. J. Rock Mech. Min. Sci. 22, 3–19.
431 https://doi.org/10.1016/0148-9062(85)92589-6
432 Ning, Y., Yang, J., An, X., Ma, G., 2011a. Modelling rock fracturing and blast-induced rock mass
433 failure via advanced discretisation within the discontinuous deformation analysis framework.
434 Comput. Geotech. 38, 40–49. https://doi.org/10.1016/j.compgeo.2010.09.003
435 Ning, Y., Yang, J., Ma, G., Chen, P., 2011b. Modelling rock blasting considering explosion gas
436 penetration using discontinuous deformation analysis. Rock Mech. Rock Eng. 44, 483–490.
437 https://doi.org/10.1007/s00603-010-0132-3
438 Onederra, I.A., Furtney, J.K., Sellers, E., Iverson, S., 2013. Modelling blast induced damage from a
439 fully coupled explosive charge. Int. J. Rock Mech. Min. Sci. 58, 73–84.

https://doi.org/10.1016/j.ijrmms.2012.10.004

Pain, C.C., Umpleby, A.P., de Oliveira, C.R.E., Goddard, A.J.H., 2001. Tetrahedral mesh optimisation and adaptivity for steady-state and transient finite element calculations. Comput. Methods Appl. Mech. Eng. 190, 3771–3796. https://doi.org/10.1016/S0045-7825(00)00294-2

Paine, A.S., Please, C.P., 1994. An improved model of fracture propagation by gas during rock blasting-some analytical results. Int. J. Rock Mech. Min. Sci. 31, 699–706. https://doi.org/10.1016/0148-9062(94)90009-4

Pavlidis, D., Gomes, J.L.M.A., Xie, Z., Percival, J.R., Pain, C.C., Matar, O.K., 2016. Compressive advection and multi-component methods for interface-capturing. Int. J. Numer. Methods Fluids 80, 256–282. https://doi.org/10.1002/fld.4078

Priest, S.D., Hudson, J. a., 1981. Estimation of discontinuity spacing and trace length using scanline surveys. Int. J. Rock Mech. Min. Sci. Geomech. Abstr. 18, 183–197. https://doi.org/16/0148-9062(81)90973-6

Rabczuk, T., Eibl, J., 2006. Modelling dynamic failure of concrete with meshfree methods. Int. J. Impact Eng. 32, 1878–1897. https://doi.org/10.1016/j.ijimpeng.2005.02.008

Saharan, M.R., Mitri, H.S., 2008. Numerical procedure for dynamic simulation of discrete fractures due to blasting. Rock Mech. Rock Eng. 41, 641–670. https://doi.org/10.1007/s00603-007-0136-9

Tarver, C.M., Breithaupt, R.D., Kury, J.W., 1997. Detonation waves in pentaerythritol tetranitrate. J. Appl. Phys. 81, 7193–7202. https://doi.org/10.1063/1.365318

Viré, A., Xiang, J., Milthaler, F., Farrell, P.E., Piggott, M.D., Latham, J.-P., Pavlidis, D., Pain, C.C., 2012. Modelling of fluid–solid interactions using an adaptive mesh fluid model coupled with a combined finite–discrete element model. Ocean Dyn. 62, 1487–1501. https://doi.org/10.1007/s10236-012-0575-z

Viré, A., Xiang, J., Pain, C.C., 2015. An immersed-shell method for modelling fluid-structure interactions. Philos. Trans. R. Soc. A Math. Phys. Eng. Sci. 373, 20140085–20140085. https://doi.org/10.1098/rsta.2014.0085

Wang, Z.L., Konietzky, H., 2009. Modelling of blast-induced fractures in jointed rock masses. Eng. Fract. Mech. 76, 1945–1955. https://doi.org/10.1016/j.engfracmech.2009.05.004

Wang, Z.L., Konietzky, H., Shen, R.F., 2009. Coupled finite element and discrete element method for underground blast in faulted rock masses. Soil Dyn. Earthq. Eng. 29, 939–945.

https://doi.org/10.1016/j.soildyn.2008.11.002

Wei, X.Y., Zhao, Z.Y., Gu, J., 2009. Numerical simulations of rock mass damage induced by underground explosion. Int. J. Rock Mech. Min. Sci. 46, 1206–1213. https://doi.org/10.1016/j.ijrmms.2009.02.007

Xiang, J., Munjiza, A., Latham, J.-P., 2009a. Finite strain, finite rotation quadratic tetrahedral element for the combined finite-discrete element method. Int. J. Numer. Methods Eng. 79, 946–978. https://doi.org/10.1002/nme.2599

Xiang, J., Munjiza, A., Latham, J.-P., Guises, R., 2009b. On the validation of DEM and FEM/DEM models in 2D and 3D. Eng. Comput. 26, 673–687. https://doi.org/10.1108/02644400910975469

Xie, Z., Pavlidis, D., Salinas, P., Percival, J.R., Pain, C.C., Matar, O.K., 2016. A balanced-force control volume finite element method for interfacial flows with surface tension using adaptive anisotropic unstructured meshes. Comput. Fluids 138, 38–50. https://doi.org/10.1016/j.compfluid.2016.08.005

Yan, P., Zhou, W., Lu, W., Chen, M., Zhou, C., 2016. Simulation of bench blasting considering fragmentation size distribution. Int. J. Impact Eng. 90, 132–145. https://doi.org/10.1016/j.ijimpeng.2015.11.015

Yang, P., 2018. High fidelity fluid-structure turbulence modeling using an immersed-body method (PhD thesis). Imperial College London, London.

Yang, P., Xiang, J., Chen, M., Fang, F., Pavlidis, D., Latham, J.-P., Pain, C.C., 2017. The immersed-body gas-solid interaction model for blast analysis in fractured solid media. Int. J. Rock Mech. Min. Sci. 91, 119–132. https://doi.org/10.1016/j.ijrmms.2016.10.006

Yang, P., Xiang, J., Fang, F., Pavlidis, D., Latham, J.-P., Pain, C.C., 2016. Modelling of fluid–structure interaction with multiphase viscous flows using an immersed-body method. J. Comput. Phys. 321, 571–592. https://doi.org/10.1016/j.jcp.2016.05.035

Yang, P., Xiang, J., Fang, F., Pavlidis, D., Pain, C.C., 2019. Modelling of fluid-structure interaction for moderate reynolds number flows using an immersed-body method. Comput. Fluids 179, 613–631. https://doi.org/10.1016/j.compfluid.2018.11.030

Yang, R., Bawden, W.F., Katsabanis, P.D., 1996. A new constitutive model for blast damage. Int. J. Rock Mech. Min. Sci. Geomech. Abstr. 33, 245–254. https://doi.org/10.1016/0148-9062(95)00064-X

500 Zhu, Z., Mohanty, B., Xie, H., 2007. Numerical investigation of blasting-induced crack initiation and
501 propagation in rocks. Int. J. Rock Mech. Min. Sci. 44, 412–424.
502 https://doi.org/10.1016/j.ijrmms.2006.09.002
503

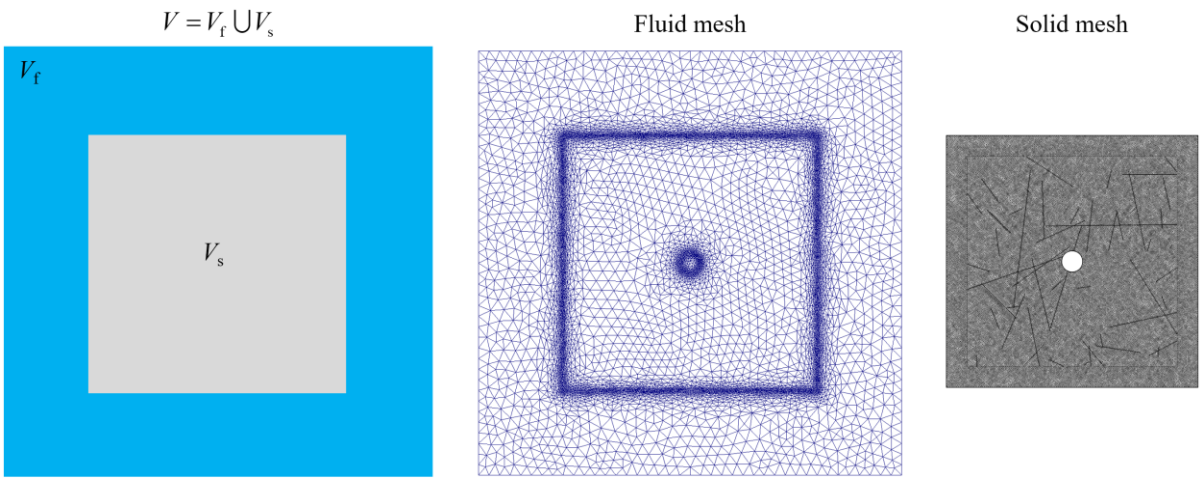
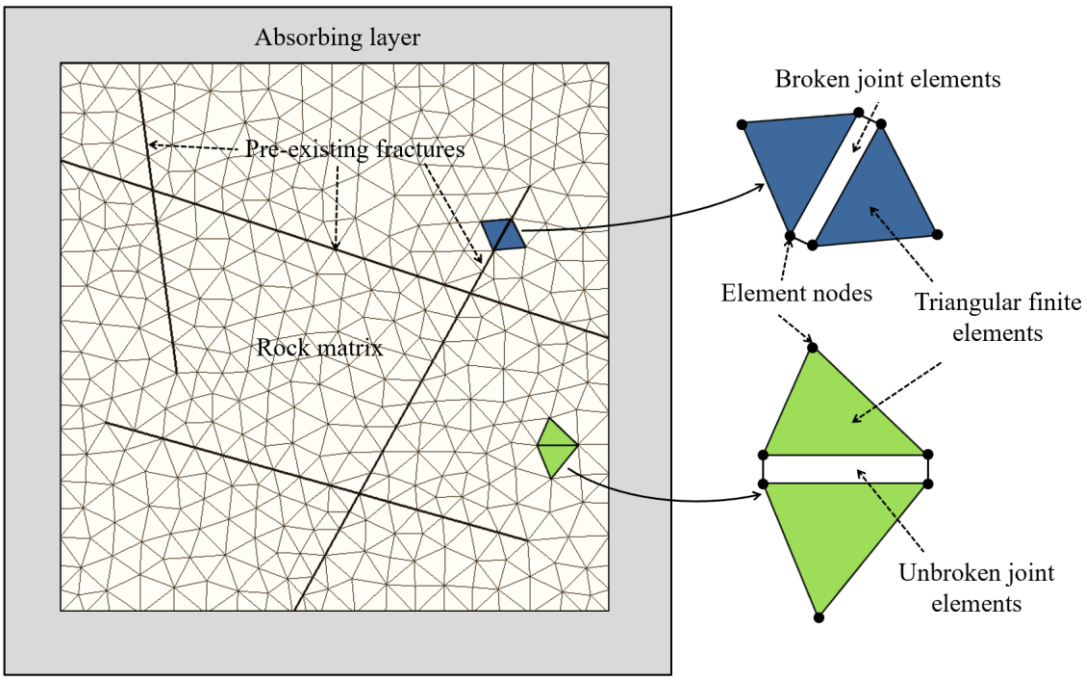


Fig. 1. Left: the computational domain V consisting of a fluid subdomain V_f and a solid subdomain V_s; middle: the fluid mesh that adapts to the volume fraction of the shell; right: the solid mesh with discretisation along pre-existing fractures.



508

509 **Fig. 2.** Representation of a fractured rock using an unstructured, fully-discontinuous mesh of

510 three-node triangular finite elements linked by four-node joint elements in the solid model.

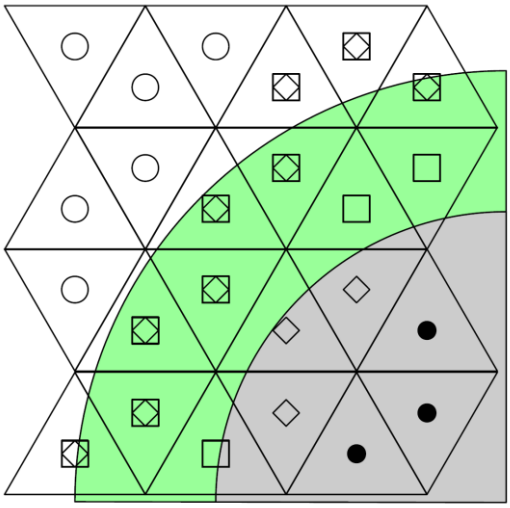


Fig. 3. Illustration of the mesh configuration in the context of the immersed-body method: the grey part is the solid mesh, the white part is the fluid mesh and the green part is the shell mesh.

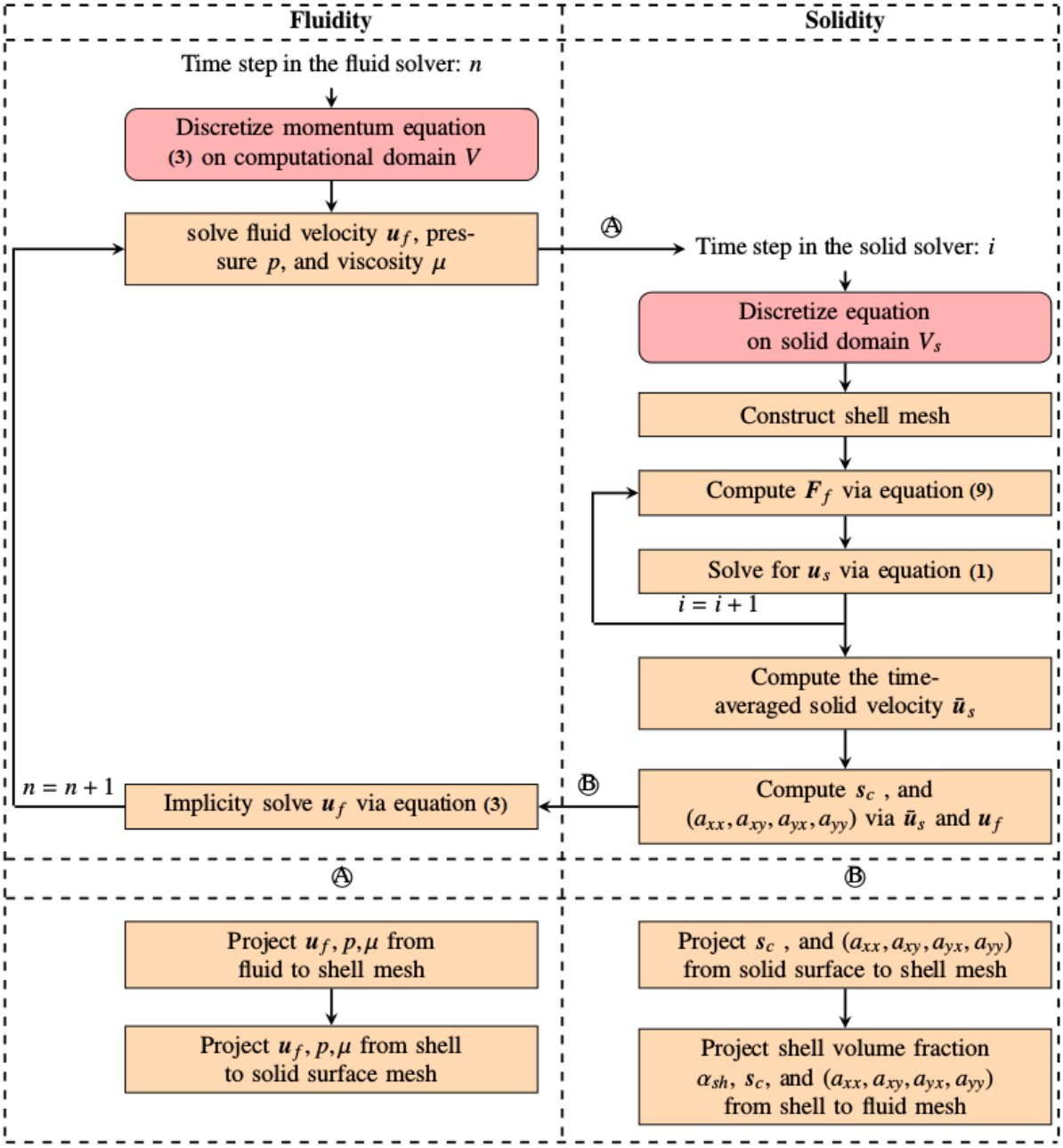
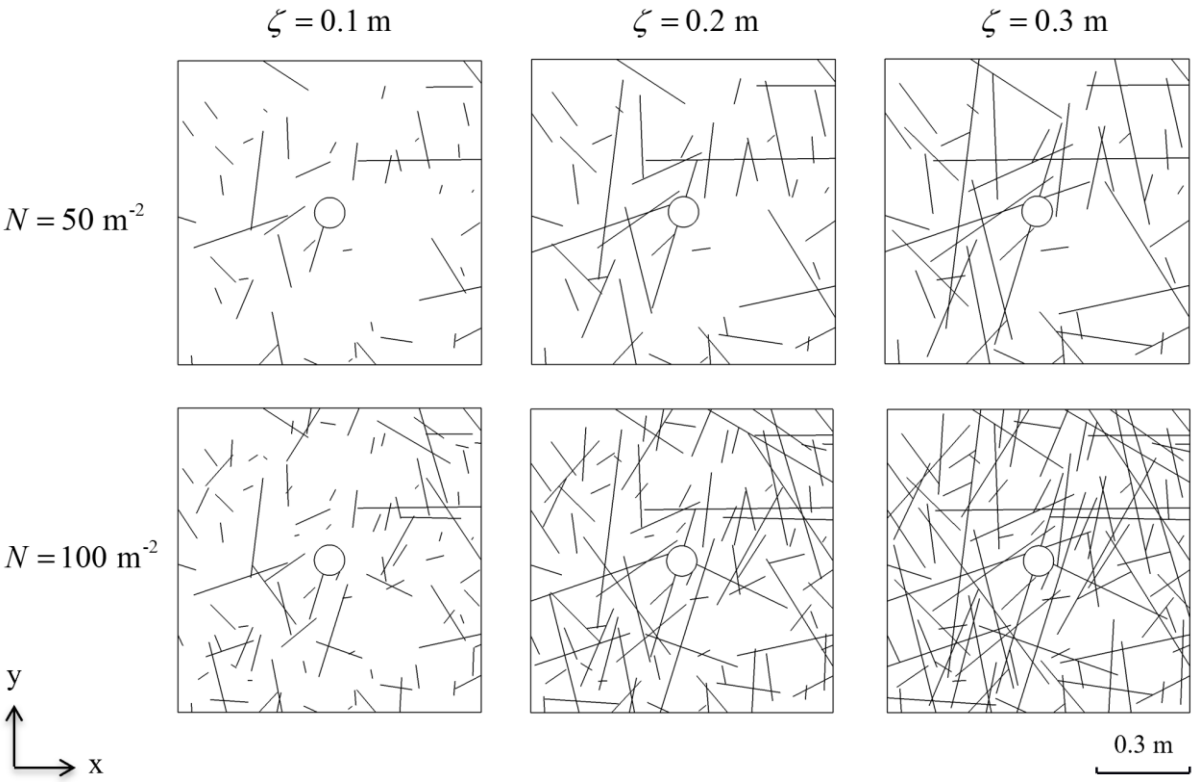


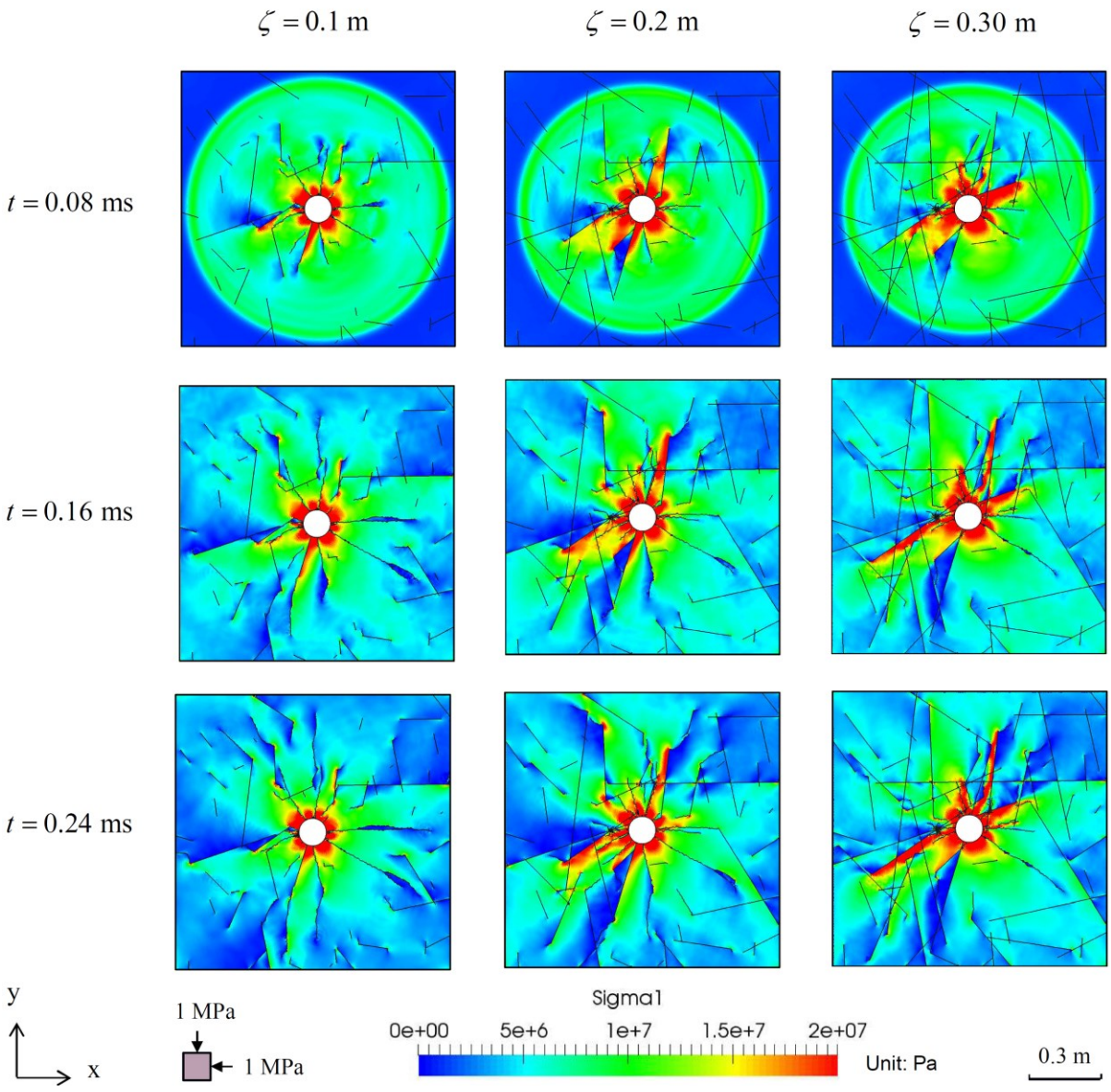
Fig. 4. Flow chart of the immersed-body method.



516

517 **Fig. 5.** The geometry of generated fracture networks (domain size L = 1 m) associated with different

518 fracture density N = 50 m^{-2} or 100 m^{-2}and different mean fracture length ζ = 0.1, 0.2 and 0.3 m.



519

520 **Fig. 6.** The variation of local maximum principal stresses during the blast-induced wave propagation

521 through the fractured rocks (1 m × 1 m) associated with a low fracture density of N = 50 m^{-2} and

522 different mean fracture length ζ = 0.1, 0.2 and 0.3 m. The fractured rock is subjected to an isotropic

523 stress loading of $S_x = S_y$ = 1 MPa.

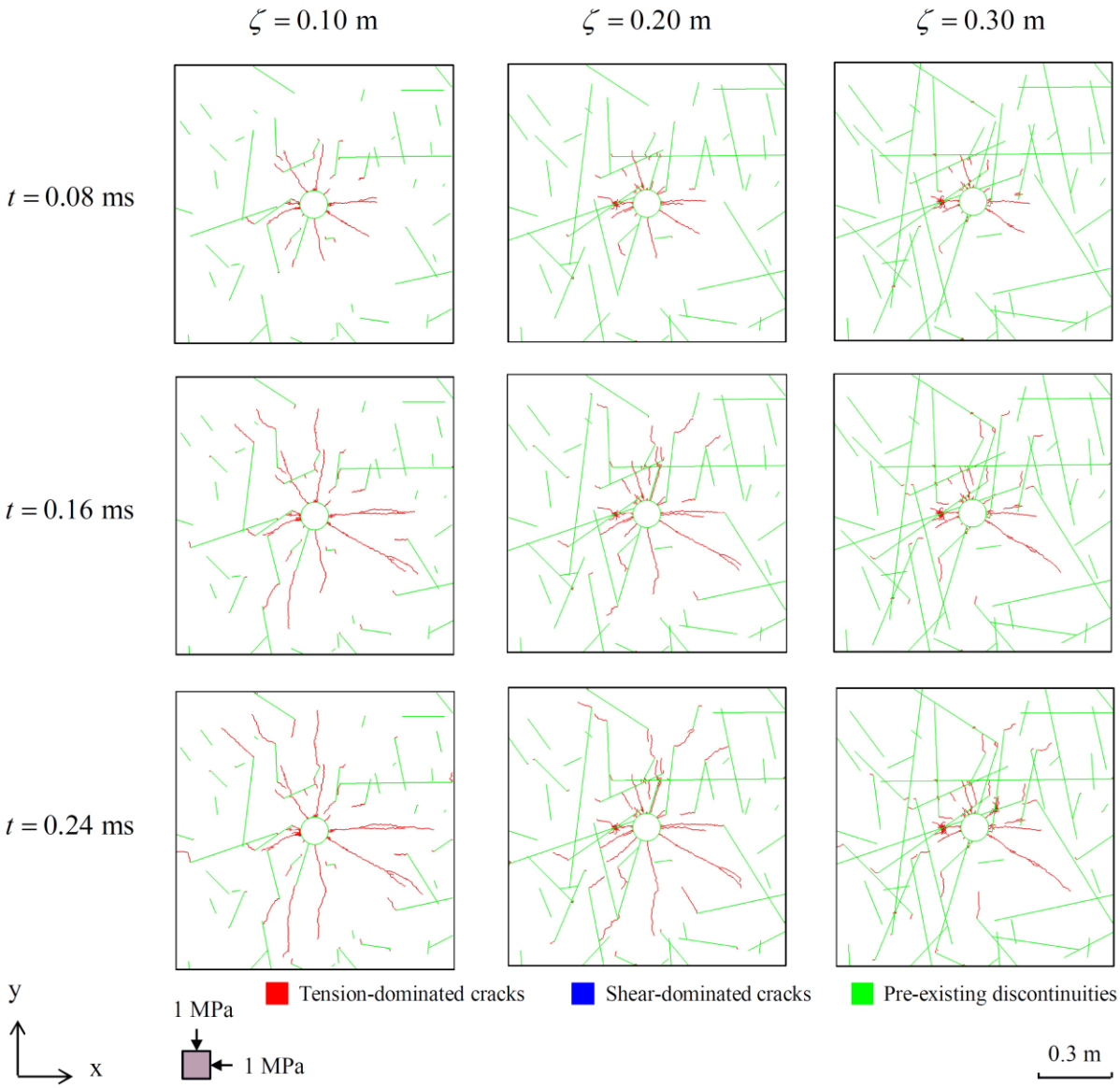
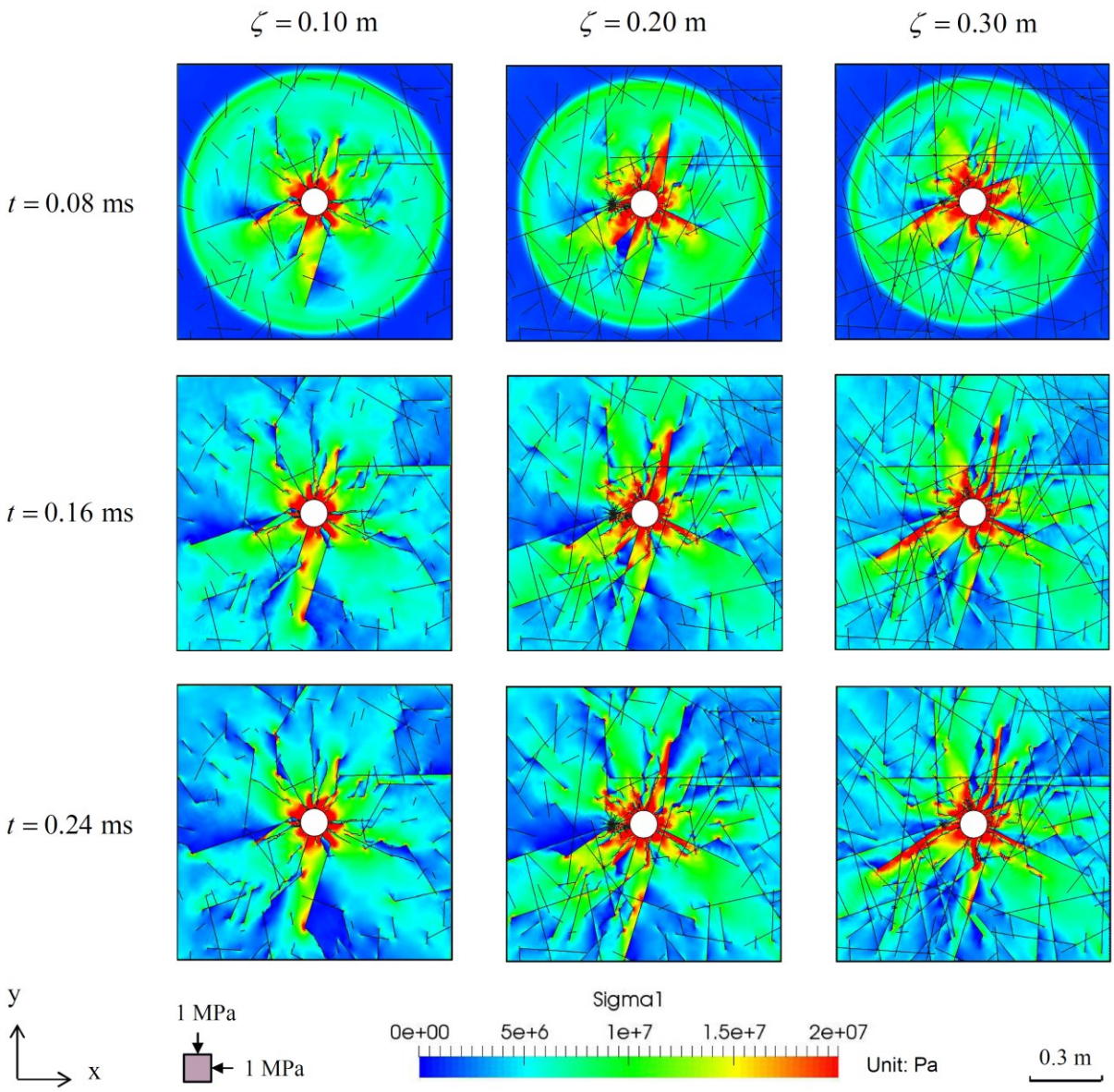


Fig. 7. The variation of fracture network geometries during the blast-induced wave propagation through the fractured rocks (1 m × 1 m) associated with a low fracture density of N = 50 m^{-2} and different mean fracture length ζ = 0.1, 0.2 and 0.3 m. The fractured rock is subjected to an isotropic stress loading of $S_x = S_y$ = 1 MPa.



529

530 **Fig. 8.** The variation of local maximum principal stresses during the blast-induced wave propagation

531 through the fractured rocks (1 m × 1 m) associated with a high fracture density of N = 100 m^{-2} and

532 different mean fracture length ζ = 0.1, 0.2 and 0.3 m. The fractured rock is subjected to an isotropic

533 stress loading of $S_x = S_y$ = 1 MPa.

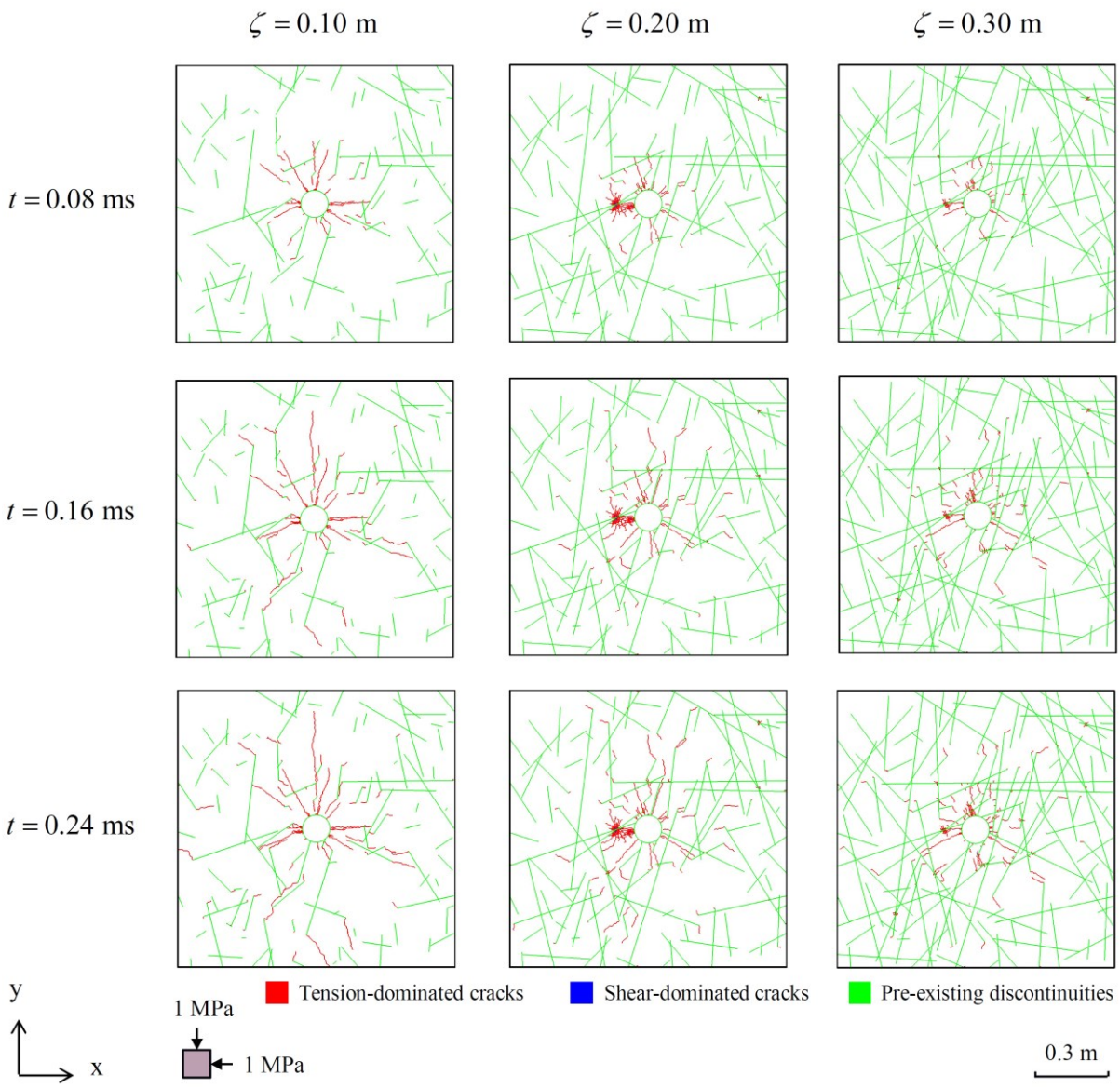
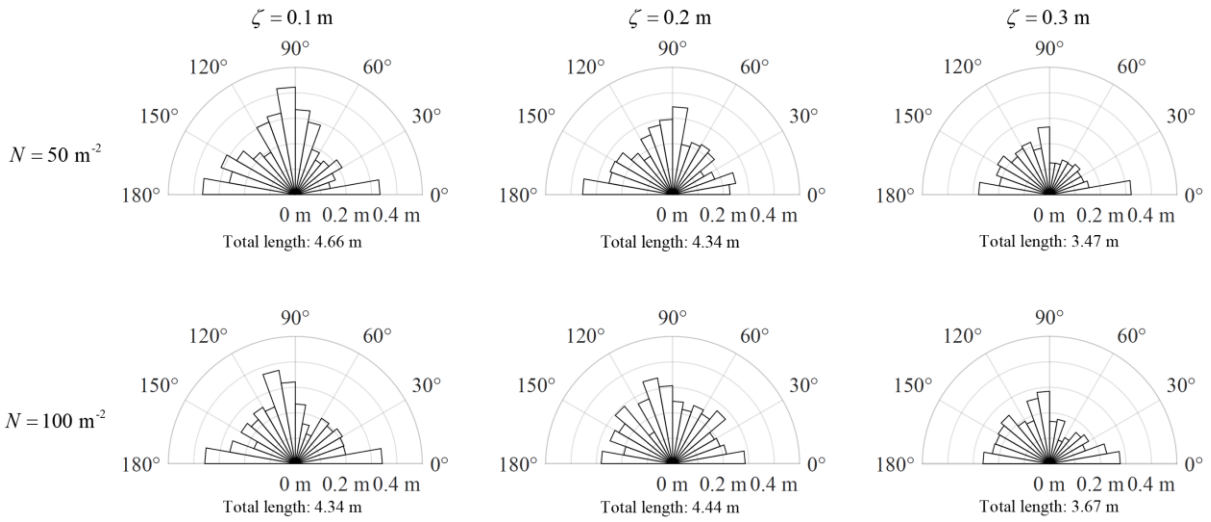


Fig. 9. The variation of fracture network geometries during the blast-induced wave propagation through the fractured rocks (1 m × 1 m) associated with a high fracture density of N = 100 m^{-2} and different mean fracture length ζ = 0.1, 0.2 and 0.3 m. The fractured rock is subjected to an isotropic stress loading of $S_x = S_y$ = 1 MPa.



539

540 **Fig. 10.** Rose diagrams of cumulative length of blast-induced cracks in different directions in the

541 fractured rocks subjected to an isotropic stress loading of $S_x = S_y = 1$ MPa.

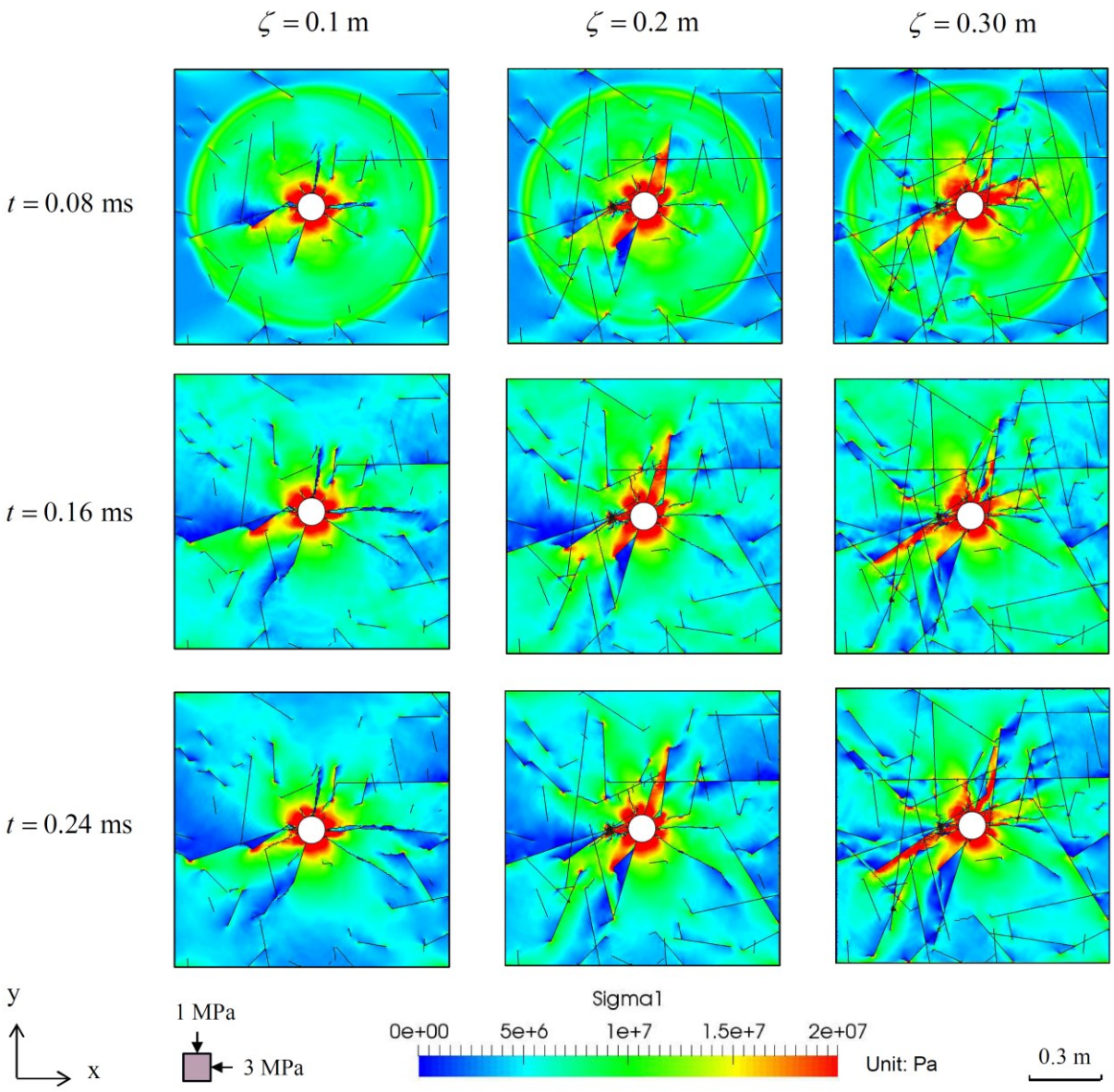
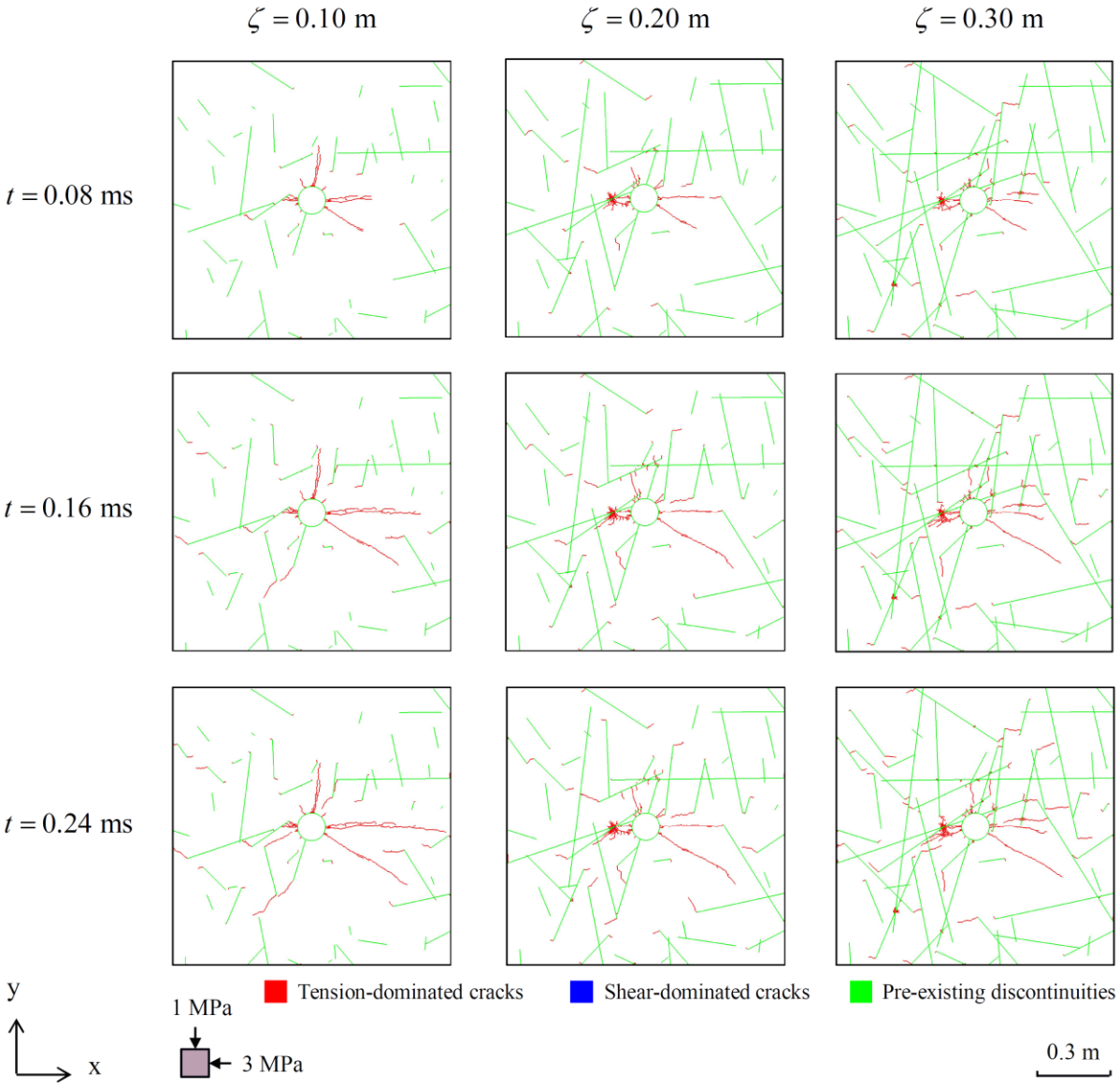
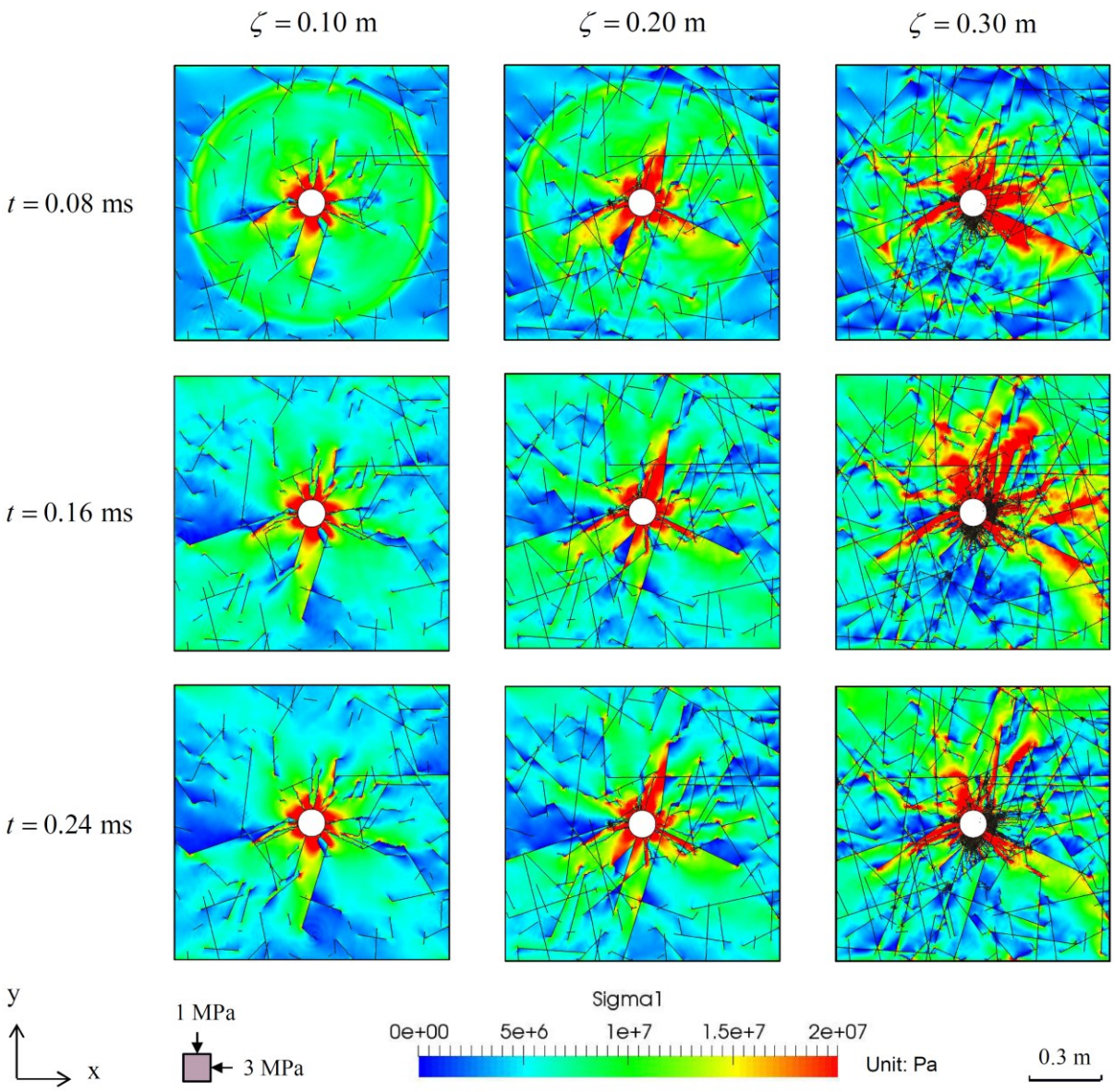


Fig. 11. The variation of local maximum principal stresses during the blast-induced wave propagation through the fractured rocks (1 m × 1 m) associated with a low fracture density of N = 50 m^{-2} and different mean fracture length ζ = 0.1, 0.2 and 0.3 m. The fractured rock is subjected to an anisotropic stress loading of S_x = 3 MPa and S_y = 1 MPa.



547

548 **Fig. 12.** The variation of fracture network geometries during the blast-induced wave propagation
549 through the fractured rocks (1 m × 1 m) associated with a low fracture density of N = 50 m^{-2} and
550 different mean fracture length ζ = 0.1, 0.2 and 0.3 m. The fractured rock is subjected to an anisotropic
551 stress loading of S_x = 3 MPa and S_y = 1 MPa.



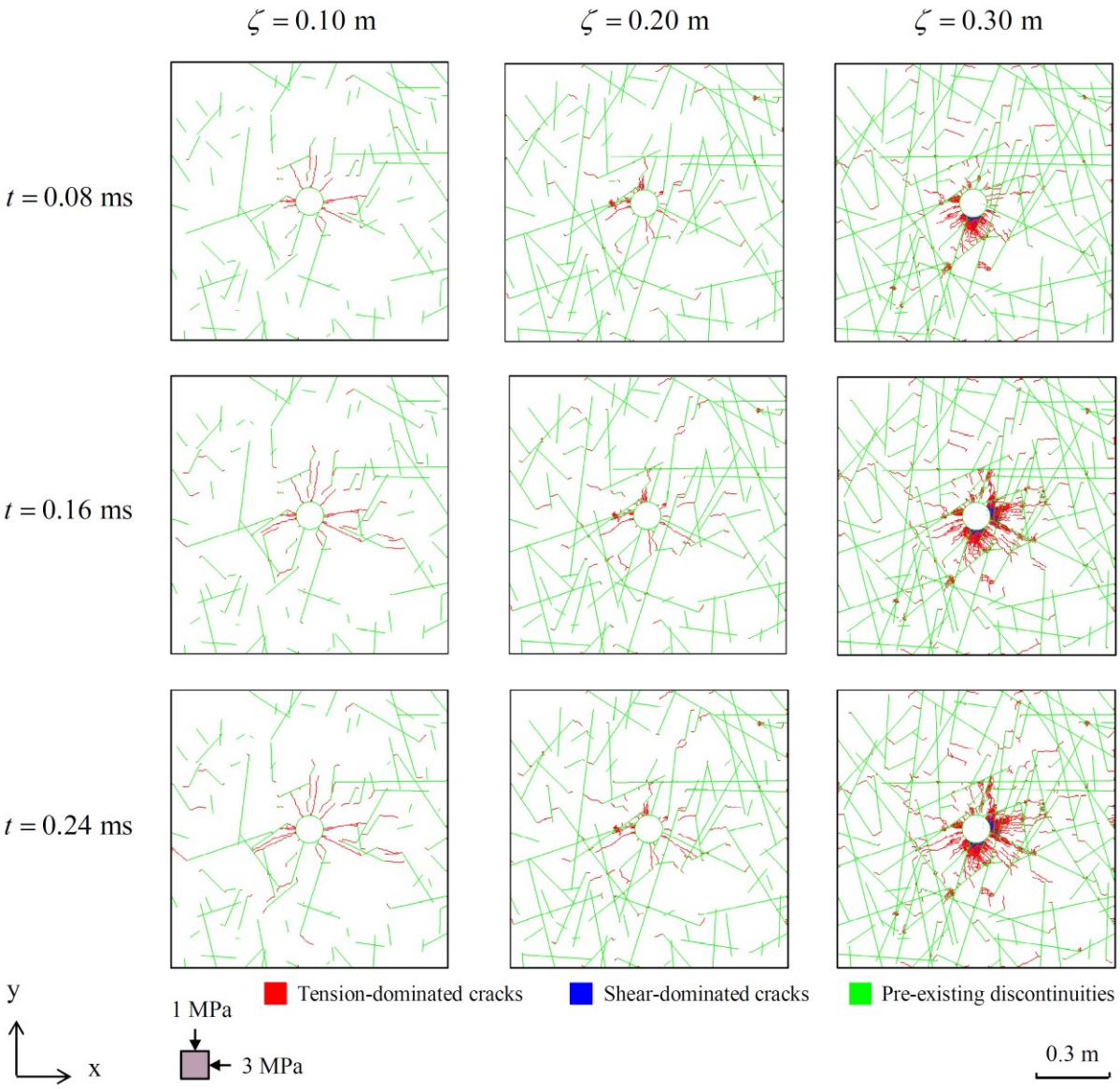
552

553 **Fig. 13.** The variation of local maximum principal stresses during the blast-induced wave propagation

554 through the fractured rocks (1 m × 1 m) associated with a high fracture density of N = 100 m^{-2} and

555 different mean fracture length ζ = 0.1, 0.2 and 0.3 m. The fractured rock is subjected to an anisotropic

556 stress loading of S_x = 3 MPa and S_y = 1 MPa.



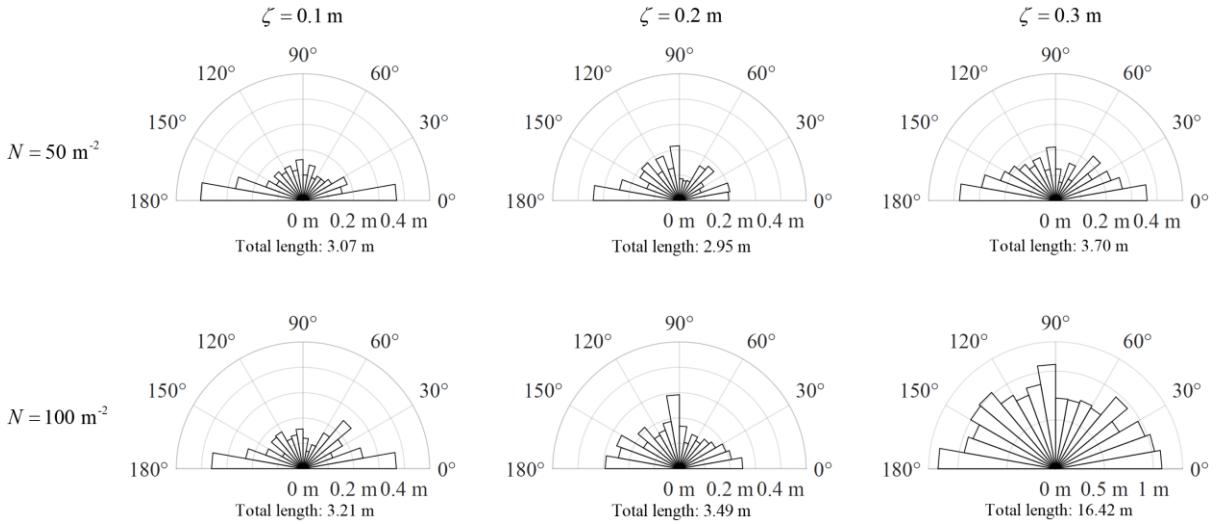
557

558 **Fig. 14.** The variation of fracture network geometries during the blast-induced wave propagation

559 through the fractured rocks (1 m × 1 m) associated with a high fracture density of N = 100 m^{-2} and

560 different mean fracture length ζ = 0.1, 0.2 and 0.3 m. The fractured rock is subjected to an anisotropic

561 stress loading of S_x = 3 MPa and S_y = 1 MPa.



562

563 **Fig. 15.** Rose diagrams of cumulative length of blast-induced cracks in different directions in the

564 fractured rocks subjected to an isotropic stress loading of S_x = 3 MPa, S_y = 1 MPa.